Magnetization textures in NiPd nanostructures

J.-Y. Chauleau,[1] B. J. McMorran,[2] R. Belkhou,[3] N. Bergeard,[1,3] T. O. Menteş,[4] M.Á. Niño,[4,*] A. Locatelli,[4] J. Unguris,[2] S. Rohart,[1] J. Miltat,[1,2,5] and A. Thiaville[1]

[1]*Laboratoire de Physique des Solides (LPS), CNRS UMR 8502, Univ. Paris-sud, FR-91405 Orsay Cedex, France*
[2]*Center for Nanoscale Science and Technology, National Institute of Standards and Technology (NIST), Gaithersburg, Maryland 20899-6202, USA*
[3]*Synchrotron SOLEIL, l'Orme des merisiers, Saint-Aubin, FR-91192 Gif-sur-Yvette, France*
[4]*ELETTRA, Sincrotrone Trieste S.C.p.A., IT-34149 Basovizza, Trieste, Italy*
[5]*Maryland NanoCenter, University of Maryland, College Park, Maryland 20742, USA*

We have observed peculiar magnetization textures in $Ni_{80}Pd_{20}$ nanostrips using three different imaging techniques: magnetic force microscopy, photoemission electron microscopy under polarized x-ray absorption, and scanning electron microscopy with polarization analysis. The appearance of diamondlike domains with strong lateral charges and of weak-stripe structures reveals the presence of both a transverse and a perpendicular anisotropy in these nanostructures. The anisotropy is seen to reinforce as temperature decreases, as testified by observations performed at 150 K. A thermal stress model with relaxation is proposed to account for these observations. Elastic calculations coupled to micromagnetic simulations support qualitatively this model.

I. INTRODUCTION

The nickel-palladium alloys (denoted here as NiPd), which form a solid solution over the whole concentration range, have been the subject of many studies for their magnetic properties.[1–4] Indeed, palladium is the $4d$ parent of nickel. It is close to being ferromagnetic according to the Stoner criterium, and forms a ferromagnetic alloy with nickel down to Ni atomic concentrations as small as $\approx 2\%$,[5,6] with a smoothly varying Curie temperature,[7] due to its large magnetic polarizability.[8] Thus, in recent years, NiPd alloys have been used as ferromagnets of tunable strength for studying the ferromagnet-superconductor proximity effect.[9] Furthermore, Pd as a noble metal has been shown to provide good electrical contacts with carbon nanotubes,[10] a property retained by the Ni-rich phase,[11] so that $Pd_{1-x}Ni_x$ ($x \approx 0.7$) has been demonstrated to perform as a good spin injector and analyzer in the study of gated spin transport in carbon nanotubes.[12,13] For such studies, NiPd occurs in the form of nanostructures, in which the magnetization orientation is expected to be controlled by the nanostructure shape and the applied field.

With soft magnetic materials such as NiFe, the magnetostatic energy (the so-called shape anisotropy) gives rise to a preferred orientation in the direction of the long edge of the nanostructure, with a coercive field that decreases as the nanostructure width increases, providing good control of the magnetization in the magnetic electrodes. For NiPd electrodes, however, this appears not to be the case. Sahoo *et al.*[11] indeed observed, when applying a field along the length of the electrodes, a progressive magnetization reversal. The switching characteristics changed completely when applying the field in the direction transverse to the electrodes,[14] as explained by the first magnetic force microscopy images obtained at LPS that constitute the starting point of this work. In these two cases, the palladium atomic concentration was 25% to 30%. Additionally, anisotropic magnetoresistance (AMR) measurements performed on electrodes (with an estimated 40% palladium content) showed that the magnetization

was very far from the longitudinal orientation.[15] From a comparison of AMR signals measured for fields oriented along several directions, that study concluded moreover that the magnetization was, on the average, tilted out of the plane. The existence of a strong perpendicular anisotropy in infinite films was also directly confirmed by ferromagnetic resonance (FMR) measurements,[15] and could also be guessed from the extraordinary Hall effect measurements on 90% Pd-rich samples.[9] In view of this complexity, we push here the study one step further by imaging the magnetization textures in the NiPd electrodes, using different magnetic imaging techniques with a high spatial resolution, namely, magnetic force microscopy (MFM), photoemission electron microscopy combined with x-ray magnetic circular dichroism (XMCD-PEEM), and scanning electron microscopy with polarization analysis (SEMPA). The possibilities and characteristics of these techniques are indeed complementary:[16] we used MFM to get a global image of the structure with no depth or component resolution, XMCD-PEEM to probe the surface magnetization componentwise and also at low temperature, and SEMPA for vectorial maps of the surface magnetization. In order to interpret quantitatively the results obtained, a model based on the differential thermal expansion of film and substrate, including elastic and micromagnetic simulations, is proposed and discussed as a cause for the observed anisotropies.

II. IMAGING AND QUALITATIVE ANALYSIS

The structures under study are Ni-rich NiPd nanostrips with varying widths w from 100 to 1000 nm and thicknesses t between 10 and 50 nm, the length being 5 μm unless otherwise specified, with a 3-nm Pd or Al cap to protect against oxidation. They have been patterned using a lift-off technique, by *e*-beam lithography and *e*-gun UHV evaporation with deposition rate around 0.13 nm/s, onto Si substrates with native oxide. The saturation magnetization ($M_S \approx 3.2 \times 10^5$ A/m) and the

typical composition have been measured by, respectively, alternating gradient force magnetometry (AGFM) and Rutherford backscattering spectroscopy (RBS), giving an atomic composition of Pd of $\approx 20\%$ (slightly drifting with source usage). Note that the following results involve only the virgin magnetization states, but that a magnetic field has also been applied, showing that the magnetization textures under study are more robust than simple metastable states generated during growth.

A. In-plane anisotropy

The MFM contrast of 30-nm thick, narrow strips [Fig. 1(a)] reveals alternate edge magnetic charges. A clear correlation between the two sides is also observed, with magnetic charges on one side facing opposite charges on the other. This regular pattern corresponds to magnetic domains with a transverse magnetization, an orientation orthogonal to the longitudinal direction that minimizes the magnetostatic energy (shape anisotropy). For slightly wider strips [Fig. 1(b)], in addition to the edge magnetic charges, an inner contrast appears. This means that the magnetization does not fully lie along the transverse axis but potentially curls inside, revealing a more complex texture (also potentially perturbed by the stray field of the MFM tip). The generality of the transverse orientation is directly attested by the image of a ring-shape sample [Fig. 1(c)]. Note also that no such magnetic structures were observed by MFM on the control unpatterned films. As MFM probes only the sample magnetic stray field (and on one side of the sample), magnetization distribution reconstruction from a MFM image is not unique. Therefore, we used two other direct imaging techniques, namely, XMCD-PEEM and SEMPA. Both techniques yield images of magnetization within a few nanometers from the surface. As the MFM images show a strong effect of the nanostrip width, the samples patterned for these techniques included a systematic variation of the nanostrip width. In addition, as the influence of the nanostrip width should be compared to that of the nanostrip thickness (at least when magnetostatics or elasticity, which have no characteristic length, come into play), samples with different thicknesses were also prepared.

The XMCD-PEEM experiments were carried out with the combined PEEM-LEEM (low-energy electron microscope) apparatus operating at the Nanospectroscopy beamline of the Elettra synchrotron,[17] the x-rays being tuned to the L_3 edge of Ni. In the setup used, the circularly polarized x rays impinge on the sample at a $16°$ angle from the surface. The differential absorption of the x rays (circular dichroism), proportional to the dot product of magnetization and photon wave vector, therefore predominantly originates from the in-plane magnetization components, with a small contribution from the out-of-plane component. The magnetization images are obtained by forming the difference of PEEM images acquired with opposite helicity of the x rays. This technique is inherently surface sensitive due to the limited electron escape depth, which is a few nanometers for the typical 2-eV energy of the collected electrons.

Figure 2 shows the images obtained on large (from 1 to 0.85 μm) and intermediate (from 0.6 to 0.45 μm) width nanostructures, for the medium thickness (30 nm). Orthogonal
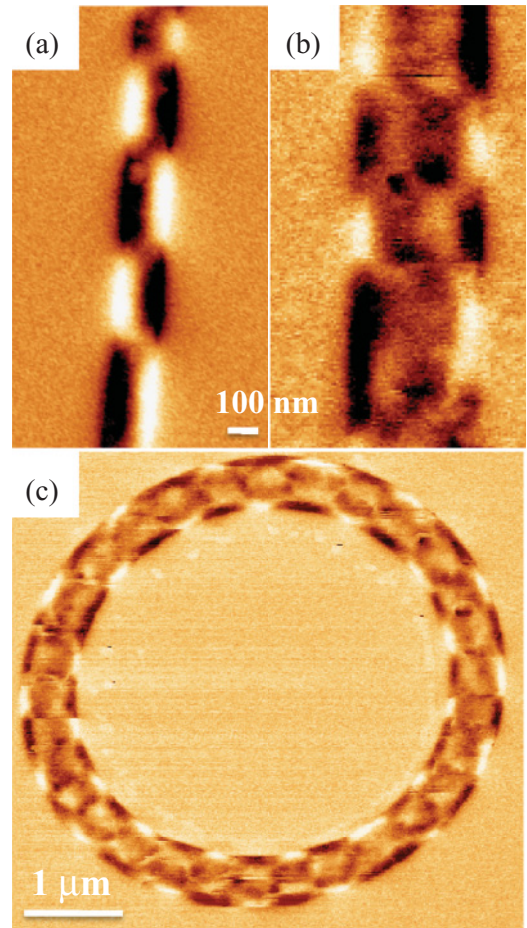

FIG. 1. (Color online) MFM images of several NiPd nanostructures with 30 nm thickness: (a) 150-nm-wide and (b) 450-nm-wide nanostrip; (c) nanoring with 500 nm width and 5 μm diameter.

sets of strips have been patterned, allowing us to probe on the same sample the transverse [Figs. 2(a) and 2(c)] and the longitudinal [Figs. 2(b) and 2(d)] components of magnetization, albeit on different structures. These magnetic images corroborate the conclusions drawn from the MFM images, as Figs. 2(a) and 2(c) show strong transverse components, with a higher complexity for the wider structures. On the other hand, a magnetic contrast is also present for images in the longitudinal configuration [Figs. 2(b) and 2(d)], proving that the magnetization is not fully transverse. For intermediate width [Fig. 2(d), 550 nm width] as well as narrower structures, symmetric diamond patterns are generally observed with no global longitudinal moment. However, deformed diamond patterns also appear [e.g., for 500 nm and 600 nm width in Fig. 2(d)], where closure domains along the long edges with one (longitudinal) magnetization are bigger than those with opposite magnetization, meaning that such structures have a nonzero longitudinal moment. For the large widths [Fig. 2(b)], this deformation is general, and very pronounced. Note, however, that the close proximity of the structures introduces a dipolar coupling, stabilizing a staggered (between successive nanostructures) longitudinal magnetization structure, quite apparent on Fig. 2(b) by the alternation of bright and dark overall contrasts. This dipolar
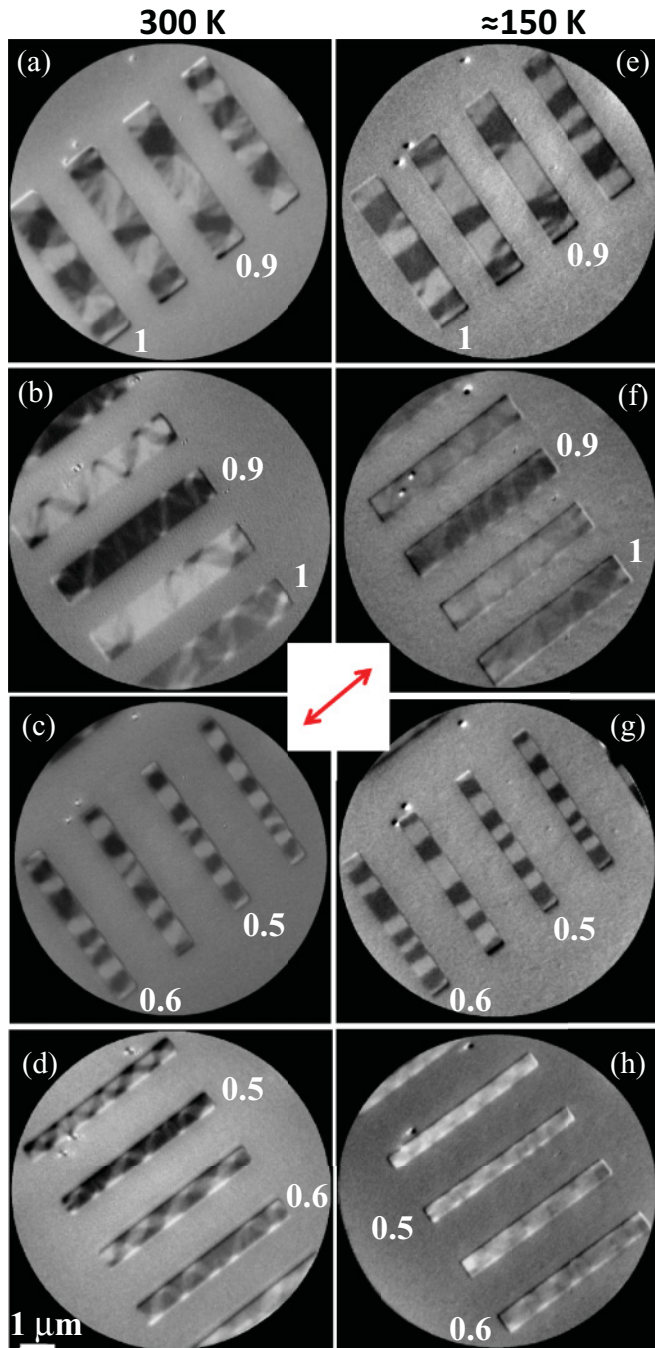
FIG. 2. (Color online) XMCD-PEEM images of four sets of 5-μm-long and 30-nm-thick structures, taken at room temperature (left column) and at low temperature ($\approx$150 K, right column). Two series of widths are shown, namely, 1 to 0.85 μm [(a), (b), (e), (f)] and 0.6 to 0.45 μm [(c), (d), (g), (h)], both with a 50-nm step (see labels on the figures). Depending on the orientation of the nanostrips with respect to the trace of the x-ray incidence plane (shown by the double arrow), the transverse [(a), (c), (e), (g)] or longitudinal [(b), (d), (f), (h)] magnetization components are probed (as these two orientations correspond to different structures, the transverse and longitudinal images for the same nanostructure width can not, however, be combined). A distortion in the electron microscope of $\approx$6 % in one direction affects the shape of the elements, and the points are defects in the imaging plate.
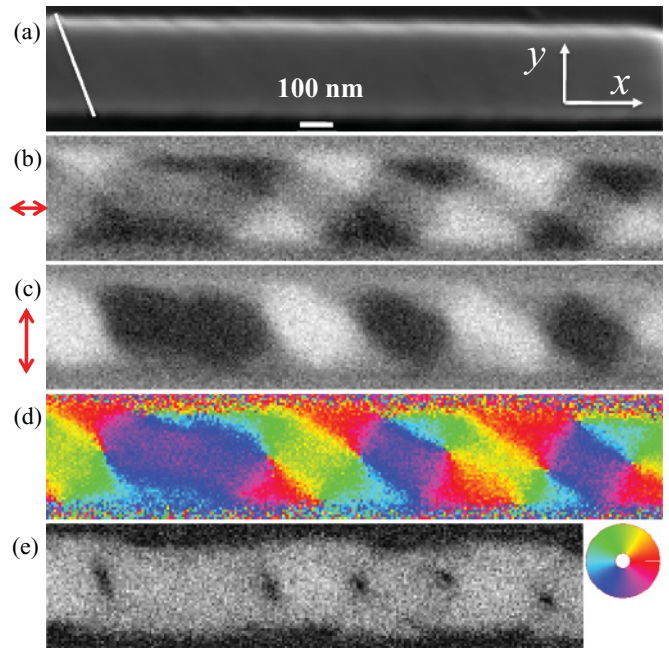

FIG. 3. (Color online) SEMPA imaging of 0.3-μm-wide and $\simeq$30$-$40-nm-thick NiPd nanostrip: (a) SEM image; (b) and (c) x and y magnetization component distributions, respectively. The processed images from (b) and (c) are (d) color-coded reconstructed vector map of the in-plane magnetization (see color wheel for the direction coding), and (e) in-plane magnetization magnitude (left part of the image only). The image distortion due to drift while scanning is schematized in (a) by the slanted orientation of the short edge of the nanostrip.

coupling gives rise to a (staggered) applied field along the longitudinal direction.

At this point, magnetization vector maps of the structures are needed. With the employed XMCD-PEEM, this requires an azimuthal sample rotation and accurate image matching. Instead, this is directly achievable using SEMPA, whereby images of the magnetization direction are obtained by measuring the spin polarization of secondary electrons emitted in the SEM. Two vector components (either the two in-plane or one in-plane and the out-of-plane component) of the surface magnetization along with the conventional SEM image are acquired simultaneously using a quadrant spin detector. For these experiments, performed on the SEMPA at NIST on initially 50-nm-thick layers, the sample surface was cleaned *in situ* by Ar ion sputtering, followed by Auger spectroscopy monitoring and capped with a few monolayers of Fe for contrast enhancement. All images discussed in the following are maps of the surface magnetization distribution resolved along the in-plane x (longitudinal) and y (transverse) axes.

Figure 3(a) displays a conventional SEM image of a 0.3-μm-wide and 10-μm-long nanostrip, attesting to the nanopatterning quality. As this sample has undergone several etching cycles, the thickness is estimated to be significantly less than the nominal 50 nm. Note that there are about 35 nm of longitudinal drift during this image scan, as seen by imaging one end of a structure, that cause the slanted shape of all images. The simultaneously measured in-plane components

of the surface magnetization are shown in Figs. 3(b) and 3(c), featuring the M_x and M_y distributions, respectively. In the longitudinal image [Fig. 3(b)], the "closure" domains where magnetization is mostly along the structure axis are highlighted. In the transverse image [Fig. 3(c)], the internal diamond-shaped domains with mostly transverse magnetization are revealed. Combining data in the x and y images yields the pixel-by-pixel orientation of the in-plane magnetization, as well as the magnitude of this in-plane component. Figure 3(d) shows the color-coded representation of the in-plane magnetization orientation. A smooth rotation between the longitudinal orientation at the borders and the transverse orientation at the nanostrip center is seen, similar to what is observed in soft materials. Thus, the transverse anisotropy can not be large compared to the magnetostatic energy. Figure 3(e) shows the magnitude of the in-plane magnetization $M_x^2 + M_y^2$. The contrast appears uniform in the image (with a noise level identical to that of the images of the two components), except at points roughly located along the strip axis. The latter clearly identify with the vortex cores, barely noticeable in MFM images. The alternate off-centered position of the vortices is another indication of a nonzero longitudinal moment of the structure (deformed diamond pattern). The uniformity of the in-plane magnetization magnitude means that, at the surface, the magnetization lies in the sample plane and the walls are of Néel type.

The images for a larger width sample (500 nm, Fig. 4) show the development of the transverse domains [Fig. 4(c)] and the relative shrinking of the closure domains [Fig. 4(b)]. The walls between transverse domains are long enough to accommodate several vortices (called Bloch lines) separating Néel wall segments [Figs. 4(b) and 4(d)]. The color-coded orientation image moreover reveals that fluctuations such as cross ties can extend from the domain walls inside the transverse domains, a phenomenon well known in soft materials,[18] which shows again that the transverse anisotropy is not very large. An arrow representation of the in-plane magnetization orientation is also shown, for the left part of the previous images, in order to provide a more direct view of the magnetization distribution [Fig. 4(e)]. Altogether, SEMPA shows that the surface magnetization is well in plane, with magnetic structures (Néel walls, Bloch lines, cross ties) that are typical of soft magnetic samples with, however, a clear transverse easy axis.

In addition, we have observed that the transverse magnetization ratio depends strongly on temperature by comparing XMCD-PEEM images at room temperature [Figs. 2(a)–2(d)] and at low temperature [$\approx$150 K, Figs. 2(e)–2(h)] on the same structures. First, comparing the transverse images [Figs. 2(a) versus 2(e), and 2(c) versus 2(g)], it is clear that the magnetic texture has been simplified when lowering temperature. The fact that intermediate gray levels have disappeared proves the reinforcement of the transverse anisotropy. This is corroborated by the loss of magnetic contrast while probing the longitudinal component [Figs. 2(b) versus 2(f), and 2(d) versus 2(h)].

B. Out-of-plane anisotropy

For the thicker structures (50 nm), an additional contrast with a fine scale appears both in the longitudinal and
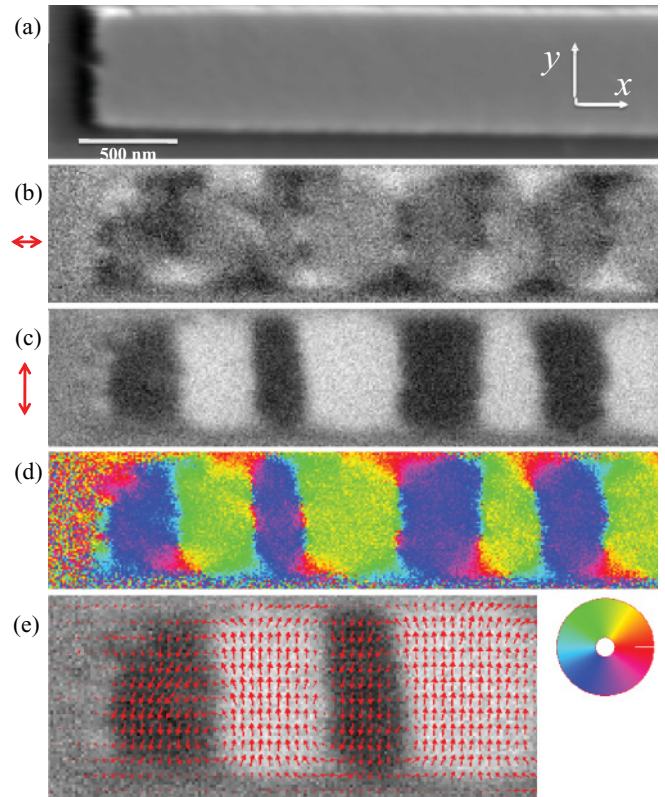

FIG. 4. (Color online) SEMPA imaging of 0.5-μm-wide nanostrip of the same sample as in Fig. 3: (a) SEM image; (b) and (c) x and y magnetization component distributions, respectively; (d) color-coded reconstructed vector map of the in-plane magnetization (see color wheel for the direction coding); (e) arrow representation of the in-plane magnetization (magnified 1.5$\times$ with respect to previous images), for the left part of the structure, on top of a background supplied by (c).

transverse configurations, which is reinforced at low temperature (Fig. 5). This contrast is also observed at room temperature by SEMPA (on nanostructures that suffered from minimal surface processing) and MFM (Fig. 6). This pattern is known as the weak-stripe domain structure (see, for example, Ref. 18 pp. 298–303), a fingerprint of an additional anisotropy with out-of-plane easy axis, the energy of which is smaller than the perpendicular demagnetization energy. In weak stripes, the magnetization at film center periodically tilts (less than 90°) out of the plane in order to decrease the perpendicular anisotropy energy. The appearance of surface charges due to this perpendicular component is avoided by creating periodic "rolls" for the magnetization components that are transverse to the main (in-plane) magnetization. Thus, the surface magnetization is mainly in plane, with a periodic partial rotation toward the direction transverse to the stripe elongation. The wave vector of these periodic rotations is orthogonal to the main magnetization direction in order to avoid magnetic charges. In the top view, weak stripes appear as domains running parallel to the main magnetization, with an oscillating transverse magnetization component (as well as with a smaller oscillating out-of-plane component with 90° dephasing). These weak stripes provide information about the magnetic structure and energetics of the sample. (i) As
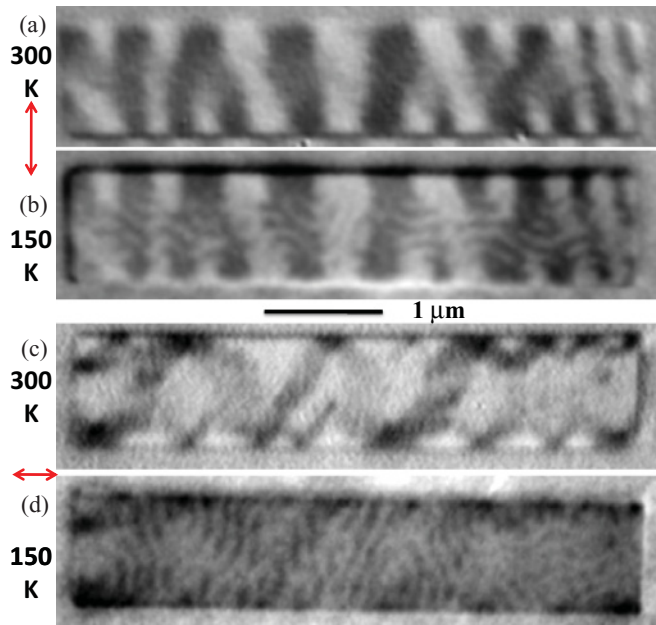
FIG. 5. (Color online) XMCD-PEEM images of two 0.9-μm-wide, 50-nm-thick NiPd nanostrips, in the transverse configuration at two temperatures: 300 K (a) and 150 K (b) and in the longitudinal configuration for the same temperatures (c), (d). Note that the same structure is observed in (a) and (b) and in (c) and (d).

XMCD-PEEM essentially probes the in-plane magnetization component, the fluctuations due to the weak-stripe structure reveal the mostly longitudinal stripes for transverse incidence and vice versa. Thus, the observation of longitudinal weak stripes in the nanostrip center [Figs. 5(b) and 6(c)], and of transverse weak stripes over all the sample width, with a reinforcement of their contrast at the long edges of the structures [Figs. 5(d) and 6(c)], shows that the magnetization is globally transverse, with longitudinal components that are largest around mid-width. (ii) Even if weak stripes are less easily observable at room temperature using XMCD-PEEM or SEMPA, MFM proves that they are present (Fig. 6) when the thickness is large enough. This feature is traced back to the surface sensitivity of XPEEM or SEMPA, compared to the volume sensitivity of MFM. Thus, the critical thickness D_{cr} at which weak stripes appear can be estimated from the MFM images. Figure 6 indeed shows that, whereas at 50 nm the stripe pattern is well established, at 30 nm nothing is observed, and at 40 nm, some modulation is barely visible, so that $D_{cr} \approx 50$ nm. This value will be later compared to calculations. (iii) Figure 6(c) indicates that the transverse anisotropy dominates close to the edges since weak stripes meet the edges at right angles. Note that, at these nanostrip dimensions, it is still possible to observe the bright and dark edge contrast, yet with no correlation anymore between the two sides. (iv) The fact that the surface magnetic contrast of the weak stripes increases at low temperatures reveals an increase of perpendicular anisotropy with respect to the demagnetizing energy.

To sum up all observations on nanostrips of varying width and thickness, a transverse anisotropy, which competes with the demagnetizing energy, has to be invoked in order to
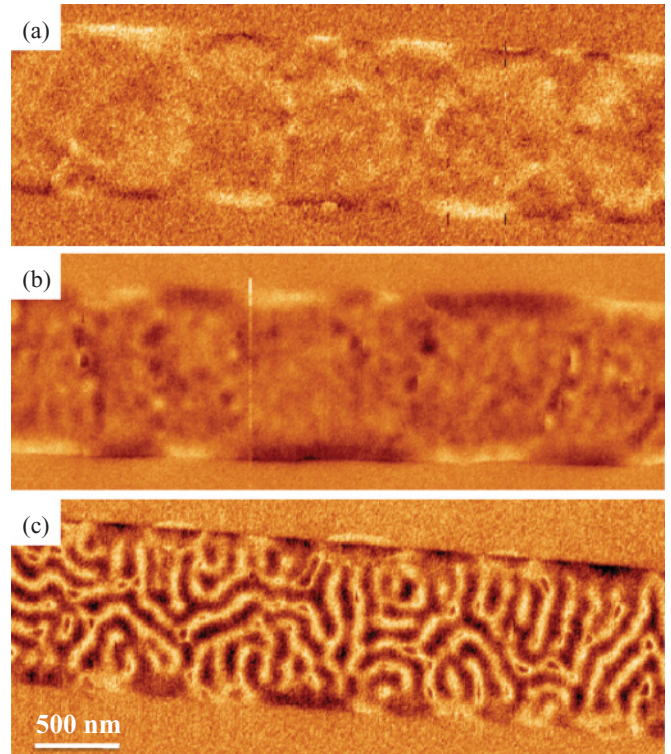

FIG. 6. (Color online) MFM images of a 1-μm-wide NiPd nanostrip, with different thicknesses: (a) 30 nm, (b) 40 nm, and (c) 50 nm, showing the appearance of the weak-stripe domain structure. In (b), the largest internal contrast appears along the domain walls between transverse domains, and is probably linked to the wall structure [see Fig. 4(b)].

maintain a stable diamond or transverse magnetic structure. In addition, we noted the presence of perpendicular anisotropy sufficient to allow for a weak-stripe pattern to appear for 50-nm-thick nanostrips. Both contributions are enhanced when temperature is decreased.

III. QUANTITATIVE ANALYSIS

We now discuss the origin of both transverse and perpendicular anisotropies. First, we note from Fig. 1(c) that the orientation of the long axis of the strips, relative either to the substrate or a deposition angle, has no noticeable effect on the observed magnetization texture. Considering the out-of-plane and edge-localized transverse anisotropies, the evolution of the magnetic contrast with temperature, and the independence of the effect on the orientation of the nanostructures, thermal stresses are a likely cause to all these phenomena. Indeed, metals and semiconductors have very different thermal expansion coefficients α, for example, $\alpha_{Ni} = 13.3 \times 10^{-6}$ K^{-1} and $\alpha_{Si} = 2.49 \times 10^{-6}$ K^{-1}. Assuming that the temperature during layer deposition is higher than room temperature, a thermal stress exists in the NiPd layer at room temperature, which is reinforced at low temperature since the temperature change reads $\Delta T = T_{growth} - T_{observation}$.

In order to evaluate quantitatively this effect, the elastic problem[19] of a nanostrip (NiPd) clamped by a substrate (Si) after cooling was numerically solved for different nanostrip transverse dimensions. As the nanostrip length is much larger
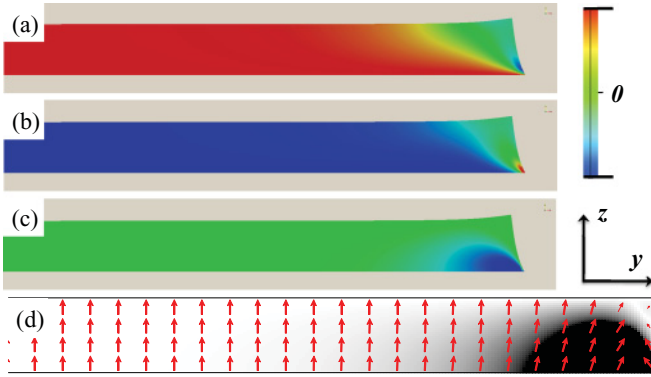
FIG. 7. (Color online) End-view cross-section representation of the thermal strain components in a 30-nm-thick and 500-nm-wide nanostrip calculated for an interfacial strain $\epsilon_0 = 10^{-3}$ (corresponding to $\Delta T = 92.5$ K for nickel), for an infinitely rigid substrate (for the meaning of axes, compare with Fig. 3). The displacements have been enhanced by a factor of 100 in order to be observable. The strain components are (a) the transverse strain ϵ_{yy}, (b) the perpendicular strain ϵ_{zz}, and (c) the shear strain ϵ_{yz}. The color scale extends between $-\epsilon_0$ and ϵ_0 for ϵ_{yy} and between $-\epsilon_1$ and ϵ_1 for ϵ_{zz} and ϵ_{yz}. A half cross section is represented because of symmetry. The anisotropy distribution is shown in (d), with arrows giving the easy axis direction and the gray levels coding the value of the transverse anisotropy, the color-code clipping values (evaluated with the nickel parameters) above 3 kJ/m^3.

than its transverse dimensions, a two-dimensional (2D) calculation was performed, corresponding to an infinite nanostrip length. This was achieved with a homemade finite differences code solving for the elastic displacement field in the framework of isotropic elasticity appropriate for polycrystalline samples. The values of the elastic coefficients of NiPd were estimated by interpolation between those published for nickel[20] and for palladium,[21] resulting in a Young's modulus $E = 187.7$ GPa and a Poisson's ratio $\nu = 0.35$. Figures 7(a)–7(c) show the distribution of the components ϵ_{ij} of the strain tensor across the right half of the section of a 30-nm-thick and 500-nm-wide nanostrip, assuming an infinitely rigid substrate. At the top edges of the nanostrip (the top right corner of the cross section), the NiPd is fully relaxed, noticeable on the maps by the zero strain regions (see color code). Along the cross-section symmetry plane, the behavior is the same as that expected for an infinite film, i.e., $\epsilon_{yy} = \epsilon_0 \equiv \Delta\alpha\Delta T$ and $\epsilon_{zz} = -2\nu/(1-\nu)\epsilon_0 \equiv -\epsilon_1$. Here, ϵ_0 is the initial interfacial strain, i.e., the product of the thermal expansion coefficient difference $\Delta\alpha$ and the temperature difference ΔT, and ϵ_1 is the perpendicular strain in an infinite film (both numbers are defined positive, but as temperature is lower than that during growth, the film is in compression along the out-of-plane direction and in tension in the plane of the interface). Besides, one can note a very localized nonzero shear strain at the bottom edges of the nanostrip [Fig. 7(c), lower right corner], which corresponds to the inclination of the lateral side of the nanostrip.

Once the strains are known, the anisotropy distribution that results from the so-called inverse magnetostriction effect[22] can be computed (see, also, Ref. 18). Note that, because of the existence of shear, this is slightly more complex than the
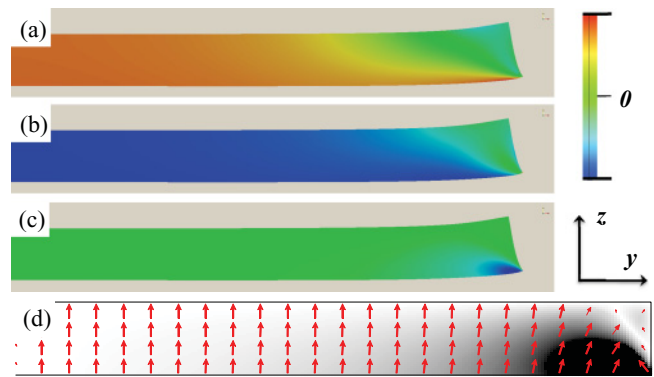

FIG. 8. (Color online) Same problem as in Fig. 7, but solved for a deformable Si substrate (treated as an isotropic medium with $E = 185$ GPa and $\nu = 0.26$) (Ref. 24). The substrate was an infinite parallelepiped with 1.5 μm edge size, with zero displacement boundary conditions applied at the three sides without structure.

textbook calculations as the magnetoelastic energy must be diagonalized at every location in order to get the local easy axis direction. The results obtained for isotropic magnetoelastic coupling with a negative magnetostriction coefficient ($\lambda_S = -36 \times 10^{-6}$ for Ni) are shown as a cross-section map in Fig. 7(d).

Since λ_S is negative, the easy axis lies along the compression axis, i.e., perpendicular to the sample plane, as already measured for Ni-rich films.[23] This is what is obtained in the middle of the strips [Fig. 7(d)]. The finite size of the strips allows strain relaxation at the edges with the appearance of shearing, driving the easy axis to locally rotate toward the transverse direction. Therefore, thermal strains do lead to out-of-plane and transverse anisotropies, which vary with position, the transverse anisotropy being a side effect of the perpendicular anisotropy. In addition, the average value of the latter will depend on the aspect ratio of the strip cross section since it rests on edge contributions. This dependence is supported by indirect magnetization measurements of some nanostrips by anisotropic magnetoresistance measurements (not shown).

The elastic calculations were repeated for a deformable Si substrate, and their results are shown in Fig. 8. The deformations in the NiPd layer are reduced, as one part of the thermal stress is relaxed in the substrate. Therefore, the induced anisotropy is reduced, but keeps roughly the same distribution.

The next step is to quantify the perpendicular anisotropy constant K_{perp}. The appearance of the weak-stripe domains provides information about this constant since the critical thickness (D_{cr}) for this depends on the quality factor $\mathcal{Q} = 2K_{\text{perp}}/\mu_0 M_S^2$.[18,25] In the present case, D_{cr} is about 50 nm. Considering an exchange constant of 0.6×10^{-11} J/m (80% of the accepted value for Ni,[26] due to dilution by Pd), we obtain an exchange length of 9.6 nm. Then, from results due to Vukadinovic *et al.*,[25] the quality factor's critical value is $\mathcal{Q} = 0.48$, corresponding to a perpendicular anisotropy constant $K_{\text{perp}} \approx 3 \times 10^4$ J/m^3. This value is of the same order of magnitude as previously obtained by FMR for infinite films.[15] The anisotropy can be linked to a difference of
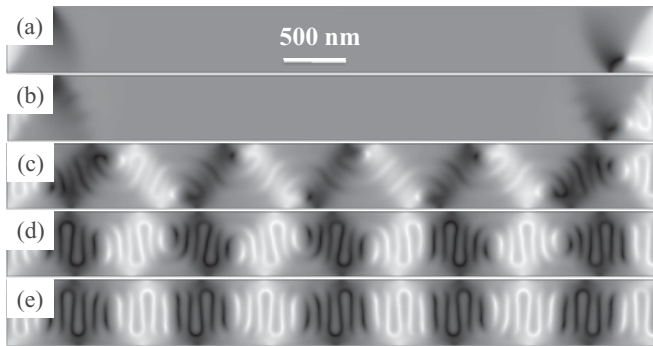
FIG. 9. Micromagnetic simulations of the equilibrium magnetization distribution (top view) in a 0.5-μm wide and 30-nm-thick nanostrip for different values of ΔT (computed with the parameters of nickel), using the anisotropy distribution shown in Fig. 7(d): (a) $\Delta T = 160$ K, (b) 250 K, (c) 260 K, (d) 270 K, and (e) 280 K. The mesh size is $5 \times 5 \times 5$ nm^3, much below the exchange length ($\Lambda \approx 9.6$ nm). The grayscale represents the magnetization transverse component, at the sample surface. As the full equilibration of the weak-stripe domains (and of the number of transverse domains) requires an infinite number of iterations, the structures shown are meaningful locally, but maybe not globally.

temperature via the following relation (valid for an infinite film):

$$K_{\text{perp}} = \frac{3}{2} \frac{E \lambda_S \Delta \alpha}{1 - \nu} \Delta T. \qquad (1)$$

Therefore, $\Delta T \approx 164$ K is needed to reach the required value when considering an isotropic elastic constant $E = 193.5$ GPa and $\nu = 0.382$ for nickel.[20] However, if we consider reported values for bulk NiPd with 20% Pd, namely, $\alpha = 16 \times 10^{-6}$ K^{-1},[27] and $\lambda_S \approx -44 \times 10^{-6}$,[28] and use the interpolated values for the elastic coefficients used in the calculations, we obtain a lower value $\Delta T \approx 116$ K.

The calculated 2D anisotropy distributions were used as inputs into the OOMMF software[29] to simulate the equilibrium magnetic structures as a function of nanostrip dimensions. Keeping a 5-μm-long strip as in the experiments, the simulation started with 11 transverse magnetic domains (as observed), and with a noise of 10% on the magnetization direction in order to avoid metastable states. Note that the anisotropy distribution, obtained for an infinitely long strip by a 2D calculation, is not correct at the x ends of the structures, so that only the internal structures should be considered. For a 50-nm-thick nanostrip, weak-stripe domains appeared (not shown), as expected.

Figure 9 presents the converged magnetic configurations in a 0.5-μm-wide and 30-nm-thick nanostrip for different values of ΔT (calculated using the parameters of nickel; they would be 1.4 times smaller with the parameters of NiPd considered here). The calculations assumed the room-temperature NiPd micromagnetic parameters; only the magnitude of the thermal-stress-induced anisotropy was scaled when changing the temperature difference ΔT. Whereas, for $\Delta T = 160$ K [Fig. 9(a)] and up to $\Delta T = 250$ K [Fig. 9(b)], the 11-domain initial state eventually becomes fully longitudinal, from $\Delta T = 260$ K [Figs. 9(c) and 9(d)], a domain structure

similar to that experimentally observed is obtained, namely, a diamondlike pattern together with off-centered vortex cores. However, the weak-stripe domain structure is very visible in the simulation contrary to experiments, revealing that the computed perpendicular anisotropy is too strong compared to the transverse term. At still higher values, for $\Delta T = 280$ K [Fig. 9(e)], a domain structure with essentially transverse domains develops, but with more visible weak stripes (this structure actually proves extremely close to observations for the same width, but 50 nm thickness). Thus, the observed structures are reproduced, but at the expense of large temperature differences, resulting in a relatively too strong perpendicular anisotropy. For the strains evaluated with substrate relaxation, the results are similar, although the stability of the transverse domains now requires $\Delta T = 320$ K (with the Ni elastic parameters).

IV. CONCLUSION AND PERSPECTIVES

In this study, the magnetization distribution of NiPd nanostrips has been imaged using complementary techniques (MFM, XMCD-PEEM, and SEMPA), revealing a transverse orientation of the magnetization and the appearance of weak stripes at large thickness. The direct observation of a largely transverse magnetization differs from the conclusions previously drawn from AMR measurements only.[15] It, however, corresponds well with the effect of field orientation on the switching of NiPd electrodes observed in magneto-transport measurements on carbon nanotubes, as reported in Refs. 11 and 14. From these observations, it appears that in order to account for the observed textures, non-negligible out-of-plane and transverse anisotropies have to be present.

Considering the evolution with temperature (increase of both anisotropy constants as temperature decreases), a thermal-stress mechanism has been considered as the origin of this surprising magnetization texture, via magnetostriction. Note that the same mechanism was invoked for explaining the spin reorientation transition observed in Ni$_{1-x}$Pd$_x$ alloys grown on Cu$_3$Au(100).[30] Performing elastic, magnetoelastic, and micromagnetic simulations, all qualitative features of the experiments could be reproduced, however, with some disagreement regarding the relative magnitudes of the transverse and out-of-plane anisotropies.

We conclude that, in addition, another effect may be present such as an interfacial strain due to metal-substrate mismatch, a structural ordering of the alloy in the growth direction (i.e., the film normal), or a plastic strain relaxation. The latter effect may also explain the observed difference in magnetic properties between the infinite film and the nanostructures, at the same thickness. Indeed, weak stripes were seen to appear at lower thickness in the nanostructures, and the value of the perpendicular anisotropy measured by ferromagnetic resonance on infinite films was smaller than deduced for nanostructures of the same thickness. This shows also that the evaluation of strain in nanostructures is difficult, and that magnetic patterns in nanostructures made out of magnetostrictive materials have to be visualized.

Even though only one composition has been considered in this study, the discussion is general and should apply

to other Pd concentrations. For lower nickel concentrations, the thermal strain is anticipated to increase, as well as the Young's modulus and magnetostriction constant (initially at least), resulting in a fairly constant induced anisotropy. On the other hand, the alloy magnetization will decrease, down to zero, so that the role of the anisotropy induced by the thermal strain will be more and more important as the nickel content decreases. As a result, the easy axis will switch to the direction perpendicular to the plane, at a temperature that depends on composition. This corresponds well to the observations at a Ni atomic concentration of 10%.[9]

Finally, similar phenomena should occur for nanostructures made of other materials with a large magnetostriction and a small saturation magnetization. Thus, this study unveils a new route for the control of magnetization orientation in nanopatterned electrodes.

*Now at Instituto Madrileño de Estudios Avanzados en Nanociencia (IMDEA Nanociencia), Cantoblanco, ES-28049 Madrid, Spain.

[1]C. Sadron, Ann. Phys. (Paris), Ser. 10, **17**, 371 (1932); Ph.D. thesis, Strasbourg University, 1932.

[2]L. Néel, Ann. Phys. (Paris), Ser. 10, **18**, 5 (1932); Ph.D. thesis, Strasbourg University, 1932.

[3]J. Crangle and W. Scott, J. Appl. Phys. **36**, 921 (1965).

[4]W. Ferrando, R. Segnan, and A. Schindler, Phys. Rev. B **5**, 4657 (1972).

[5]A. P. Murani, A. Tari, and B. R. Coles, J. Phys. F: Met. Phys. **4**, 1769 (1974).

[6]T. Kontos, M. Aprili, J. Lesueur, X. Grison, and L. Dumoulin, Phys. Rev. Lett. **93**, 137001 (2004).

[7]M. Hansen, *Constitution of Binary Alloys* (McGraw-Hill, New York, 1958).

[8]J. Vogel, A. Fontaine, V. Cros, F. Pétroff, J.-P. Kappler, G. Krill, A. Rogalev, and J. Goulon, Phys. Rev. B **55**, 3663 (1997).

[9]T. Kontos, M. Aprili, J. Lesueur, and X. Grison, Phys. Rev. Lett. **86**, 304 (2001).

[10]A. Javey, J. Guo, Q. Wang, M. Lundstrom, and H. Dai, Nature (London) **424**, 654 (2003).

[11]S. Sahoo, T. Kontos, C. Schönenberger, and C. Sürgers, Appl. Phys. Lett. **86**, 112109 (2005).

[12]S. Sahoo, T. Kontos, J. Furer, C. Hoffmann, M. Gräber, A. Cottet, and C. Schönenberger, Nat. Phys. **1**, 99 (2005).

[13]H. T. Man, I. J. W. Wever, and A. F. Morpurgo, Phys. Rev. B **73**, 241401(R) (2006).

[14]C. Feuillet-Palma, T. Delattre, P. Morfin, J. M. Berroir, G. Feve, D. C. Glattli, B. Plaçais, A. Cottet, and T. Kontos, Phys. Rev. B **81**, 115414 (2010).

[15]J. C. Gonzalez-Pons, J. J. Henderson, E. del Barco, and B. Ozyilmaz, Phys. Rev. B **78**, 012408 (2008).

[16]H. Hopster and H. P. Oepen, *Magnetic Microscopy of Nanostructures* (Springer, Berlin, 2005).

[17]A. Locatelli, L. Aballe, T. Mentes, M. Kiskinova, and E. Bauer, Surf. Interface Anal. **38**, 1554 (2006).

[18]A. Hubert and R. Schäfer, *Magnetic Domains* (Springer, Berlin, 1998).

[19]S. Timoshenko and J. N. Goodier, *Theory of Elasticity* (McGraw Hill, New York, 1970).

[20]M. Yamamoto, Sci. Rep. Res. Inst. Tohoku Univ., Ser. A **3**, 308 (1951).

[21]J. Rayne, Phys. Rev. **118**, 1545 (1960).

[22]S. Chikazumi, *Physics of Magnetism* (Wiley, New York, 1964).

[23]J. Ben Youssef, N. Vukadinovic, D. Billet, and M. Labrune, Phys. Rev. B **69**, 174402 (2004).

[24]J. Wortman and R. Evans, J. Appl. Phys. **36**, 153 (1965).

[25]N. Vukadinovic, M. Labrune, J. Ben Youssef, A. Marty, J. C. Toussaint, and H. Le Gall, Phys. Rev. B **65**, 054403 (2001).

[26]H. Kronmüller, *Handbook of Magnetism and Advanced Magnetic Materials* (Wiley, New York, 2007), pp. 703–741.

[27]H. Masumoto and S. Sawaya, Trans. Jap. Inst. Met. **11**, 391 (1970).

[28]T. Tokunaga and H. Fujiwara, J. Phys. Soc. Japan **45**, 1232 (1978).

[29]OOMMF is a free software (in fact, an open framework for micromagnetics routines) developed by M. J. Donahue and D. Porter mainly, from NIST. It is available at [http://math.nist.gov/oommf].

[30]F. Matthes, M. Seider, and C. Schneider, J. Appl. Phys. **91**, 8144 (2002).